



Amorphization-induced reverse electron transfer in NiB cocatalyst for boosting photocatalytic H₂ production

Haoyu Long ^a, Duoduo Gao ^b, Ping Wang ^{b,*}, Xuefei Wang ^b, Feng Chen ^b, Huogen Yu ^{a,b, **}

^a Laboratory of Solar Fuel, Faculty of Materials Science and Chemistry, China University of Geosciences, Wuhan 430074, PR China

^b State Key Laboratory of Silicate Materials for Architectures and School of Chemistry, Chemical Engineering and Life Sciences, Wuhan University of Technology, Wuhan 430070, PR China



ARTICLE INFO

Keywords:

Photocatalytic H₂ evolution
Reverse electron transfer
Amorphous NiB cocatalyst

ABSTRACT

Regulating the electron density distribution of active sites to accelerate catalytic process is of great significance to explore high-efficiency cocatalysts for photocatalytic hydrogen production. In this work, a novel strategy of amorphization-induced reverse electron transfer is proposed to optimize the electronic structure of Ni active site in nickel boride (NiB) cocatalyst to promote the photocatalytic hydrogen-production activity of TiO₂. Herein, the NiB nanodots (0.5–1 nm) with an amorphous structure can perfectly be anchored onto TiO₂ surface via a novel-designed light-induced route. The resulting amorphous-NiB/TiO₂ sample achieves the photocatalytic H₂-production rate of 2334.0 μmol h⁻¹ g⁻¹, which is 1.8 times higher than that of the traditional crystalline-NiB/TiO₂ photocatalyst. The experimental and theoretical investigations confirm that the amorphization of NiB can induce the reverse electron transfer from B to Ni, which can promote the hydrogen desorption process of the Ni active site to boost the H₂-production efficiency. This work paves a new way for active site optimization and delivers in-depth insights for the exploration of high-efficient hydrogen-production cocatalysts.

1. Introduction

Solar-driven hydrogen (H₂) production over photocatalysts (TiO₂, g-C₃N₄, ZnIn₂S₄, etc.) is an environmentally benign technique to assist the sustainable energy system [1–6]. However, the photocatalytic H₂-evolution activities of the photocatalysts are inevitably suppressed by the rapid recombination of photoexcited electrons and sluggish interfacial H₂-generation reaction kinetics [7–10]. As a widely employed strategy, cocatalyst modification can eloquently promote the activities of the above bare photocatalysts by separating the photocarriers and providing reactive sites for the interfacial hydrogen production reaction [11–14]. As for the H₂-evolution reaction, the hydrogen adsorption/desorption balance on the active sites of cocatalysts should be simultaneously appropriate for fast-capturing atomic hydrogen in the medium and rapidly releasing H₂ to achieve overall high-efficiency H₂ production [15–19]. Unfortunately, the active sites in most studied cocatalysts still exhibit undesirable hydrogen adsorption owing to their inferior electronic configurations, resulting in their limited catalytic activities [20–22]. Therefore, it is essentially important to explore strategies to optimize the electron density distribution of the cocatalyst to optimize

the hydrogen adsorption/desorption balance of the active site for efficient photocatalytic hydrogen production.

At present, transition metal borides (TMBs) have received wide concern in the field of catalysis due to their metalloid electrical conductivity, component adjustability and good thermal stability [23–27]. In particular, nickel boride (NiB) has been widely employed as an effective electrocatalytic water-splitting catalyst because of its low cost and easy accessibility [28–30], and the metallic Ni sites are considered to be the active sites for hydrogen evolution [31,32]. It was reported that the metallic Ni atom on Ni metal cocatalyst usually possesses a strong H adsorption capacity [33,34], which is unfavorable for H₂ desorption in the hydrogen evolution process (Fig. 1a) [35,36]. Unfortunately, after the combination of Ni metal with B to produce crystalline NiB, the Ni active sites inevitably possess an electron-deficient state due to the electron transfer from Ni to B according to Pauling's electronegativity rule, resulting in a stronger H adsorption and slower hydrogen desorption on the Ni site (Fig. 1b) [37,38]. To improve the H₂-evolution performance of NiB, considerable efforts have been devoted to regulating the electron density distribution of the NiB to optimize the hydrogen desorption on Ni site, such as heterostructure construction and

* Correspondence to: Chemical Engineering and Life Sciences, Wuhan University of Technology, Wuhan 430070, China.

** Correspondence to: Faculty of Materials Science and Chemistry, China University of Geosciences, Wuhan 430074, China.

E-mail addresses: wangping0904@whut.cn (P. Wang), yuhogen@cug.edu.cn (H. Yu).

heteroatoms introduction [39,40]. For example, it has been recently reported that the construction of $\text{Ni}_3\text{B}/\text{Ni}$ [41,42] and $\text{Ni}_3\text{B}/\text{MoB}$ [43] heterojunctions could weaken the hydrogen adsorption of Ni active sites by regulating the electron arrangements at the grain boundaries to promote the H_2 -evolution performance. Another wide-employed strategy is heteroatom doping, such as reported NiCoB [44] and NiFeCoB [45], in which the introduced Fe and Co atoms can optimize the hydrogen desorption of neighbored Ni active sites by donating electrons to Ni. However, the above traditional strategies about the heterostructure construction and heteroatom integration would inevitably suffer from the interference of external substances, which will lead to the decreased stability of the catalytic materials [46]. Therefore, it is urgently vital to develop a sustainable, high-efficient and atom-economic strategy to modulate the electron density distribution of Ni active site in NiB.

Compared with the crystalline structure, it was reported that the amorphization of materials could disturb or even reconstruct the electron density distribution of the active sites by endowing the active sites with appropriate coordination environment [47]. It can be envisioned that the above electronic configuration adjustment by amorphization strategy can dramatically facilitate the catalytic properties of active sites. Unfortunately, this relative strategy is rarely reported in the catalytic field. Motived by the above concerns, we here present a new strategy of amorphization-induced reverse electron transfer from B to Ni in amorphous NiB, with the purpose of optimizing the hydrogen desorption of Ni active sites in NiB cocatalyst to promote the photocatalytic H_2 -generation activity of TiO_2 (Fig. 1c). In this case, the amorphous NiB (a-NiB) with ultrasmall particle size (0.5 nm) can uniformly be deposited on TiO_2 surface to synthesize a-NiB-modified TiO_2 photocatalyst (a-NiB/ TiO_2) via a novel well-designed photodeposition route. Photocatalytic H_2 -evolution tests found that the a-NiB/ TiO_2 (8%) photocatalyst displayed the optimal activity of $2344.0 \mu\text{mol h}^{-1} \text{g}^{-1}$, which is superior to the conventional crystalline NiB-modified TiO_2 (c-NiB/ TiO_2) photocatalyst. XPS investigations and Density Functional Theory (DFT) calculations affirm the reverse electron transfer from B to Ni in the amorphous NiB compared with the conventional crystalline NiB cocatalyst, which can efficiently promote the hydrogen desorption of Ni active sites, thereby boosting the hydrogen-production performance of TiO_2 . To the best of our knowledge, this is the first report on the amorphization-induced reverse electron transfer in the internal NiB for improved photocatalytic hydrogen production. The present amorphization-induced optimization of active sites offers a significant conception to design high-efficient cocatalysts for photocatalytic hydrogen production.

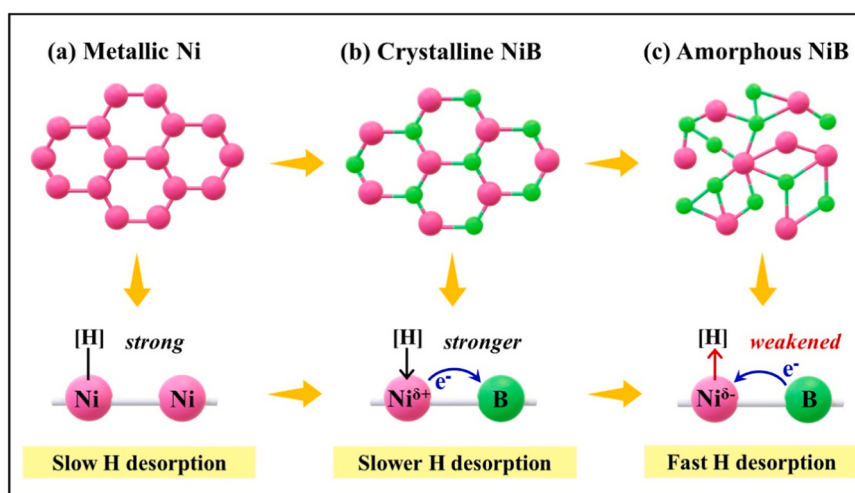


Fig. 1. The strategy for amorphization of NiB cocatalyst to optimize the H desorption for H_2 production via reversing electron transfer: (a) metallic Ni, (b) crystalline NiB and (c) amorphous NiB.

2. Experimental sections

2.1. Preparation of a-NiB/ TiO_2 photocatalyst

The a-NiB/ TiO_2 photocatalysts were prepared by in-situ formation of amorphous NiB on TiO_2 surface via a direct light-induced route. Specifically, 100 mg of TiO_2 powder was first dispersed into 80 mL EtOH solution (25 vol%) to form a suspension, and then a certain amount of Ni (CH_3COOH)₂ was dissolved into the above suspension under ultrasound. Subsequently, 2 mL of 0.5 M dimethylamine borane (DMAB) solution was injected into the above suspension with magnetic stirring for 10 min. After that, the above system was fully degassed with N_2 for 15 min and irradiated with 4 LED lights (365 nm) to trigger the photodeposition of amorphous NiB on TiO_2 surface. After illuminating for 2 h, the products were filtered, washed and vacuum dried at 55 °C to obtain the a-NiB/ TiO_2 photocatalysts. Herein, the weight percentage of Ni element to TiO_2 was set to be 1, 3, 5, 8, 10, and 12 wt%, and the obtained products were named a-NiB/ TiO_2 -X, where X represented 1, 3, 5, 8, 10, and 12, respectively. For comparison, the crystalline NiB-modified TiO_2 photocatalyst (c-NiB/ TiO_2) was gained by directly calcining the above a-NiB/ TiO_2 sample at argon atmosphere (300 °C, 2 h).

2.2. Characterization

The crystal phase properties and morphologies for various samples were analyzed via X-ray diffraction (XRD, Rigaku III), scanning electron microscope (SEM, JSM-7500 F), and transmission electron microscope (TEM, Thermo Fisher). The composition and valence states of elements in the samples are investigated using inductively coupled plasma-optical emission spectrometry (ICP-OES, Agilent 730), ex-situ X-ray photoelectron spectroscopy and in-situ irradiated X-ray photoelectron spectroscopy (XPS, ESCALAB 250Xi). All the XPS binding energies were calibrated by the adventitious carbon C 1 s peak at 284.8 eV. The ultraviolet-visible absorption spectra (UV-vis) were recorded by using a UV-2450 instrument. The time-resolved photoluminescence (TRPL) spectra were collected on a fluorescence lifetime spectrophotometer (FLS920).

2.3. Photocatalytic H_2 evolution test

The H_2 -evolution experiments of the photocatalysts were performed in a 100 mL three-neck flat-bottom Pyrex flask at ambient temperature and atmospheric pressure, and the outlets of the flask were sealed with a

silicone rubber septum, which is in line with the previous reports [13, 19]. In a typical measurement, 0.05 g of the prepared photocatalyst was dispersed in an aqueous solution with the addition of lactic acid as the sacrificial agent (80 mL, 10 vol%). Then, the flask containing the photocatalyst suspension was subjected to magnetic stirring and ultrasonic treatment, respectively. After purging with nitrogen (15 min), the resulting reactor was illuminated by 4 LED lamps (3 W 365 nm) to realize the photocatalytic H₂ production. After periodical irradiation for 30 min, a gas chromatograph (GC-2014 C) was employed to calculate the amount of generated H₂ to analyze the activities of various photocatalysts.

3. Results and discussion

3.1. Synthetic strategy of *a*-NiB/TiO₂ photocatalyst

The amorphous NiB nanodots are mildly fabricated and synchronously anchored on TiO_2 surface via a photo-triggered electron-reduction route (Fig. 2). Firstly, TiO_2 nanoparticles are dispersed into $\text{Ni}(\text{Ac})_2$ solution to form a uniform suspension, and the positive divalent nickel ions can easily be accumulated on TiO_2 surface via the electrostatic interaction to form $\text{Ni}^{2+}/\text{TiO}_2$ (Fig. 2a-(1)) [48]. When DMAB is injected to the above system, DMAB can combine the Ni^{2+} on TiO_2 surface to form $[\text{Ni}(\text{DMAB})]^{2+}$ via a chemical complexation attraction, which can be well evidenced by the following UV-visible adsorption results in Fig. 2b [49,50]. In this case, the $[\text{Ni}(\text{DMAB})]^{2+}$ complex displays an obviously shifted adsorption peak compared to the single Ni^{2+} and DMAB solution, strongly verifying the excellent combination of Ni^{2+} and

DMAB on TiO_2 surface to form $[\text{Ni}(\text{DMAB})]^{2+}/\text{TiO}_2$ (Fig. 2a-(2)). Subsequently, after the excitation of UV light (Fig. 2a-(3)), the massive $[\text{Ni}(\text{DMAB})]^{2+}$ species can finally be *in situ* reduced to form amorphous NiB nanodots (a-NiB) on TiO_2 surface to gain a-NiB/ TiO_2 photocatalyst (Fig. 2a-(4)). Herein, the reductive photoelectron excited by light from TiO_2 can effectively transfer to the surface and induce the mild reduction of $[\text{Ni}(\text{DMAB})]^{2+}$ complex to form amorphous NiB nanodots on TiO_2 surface (Fig. 2c). The photographs of the color change in different photodeposition stages are shown in Fig. 2d. It can be easily found that compared with the gray color of Ni/TiO_2 suspension (Figs. 2d-(1)), the a-NiB/ TiO_2 system (Fig. 2d-(2)) apparently exhibits the dark black after photodeposition, implying the successful realization of black a-NiB cocatalyst on TiO_2 surface to form a-NiB/ TiO_2 photocatalyst. By controlling the different concentrations of $\text{Ni}(\text{Ac})_2$ solution, the a-NiB/ TiO_2 photocatalyst with various loading amounts of a-NiB cocatalyst can be successfully and precisely prepared through the foregoing photodeposition route.

3.2. Microstructures of α -NiB/TiO₂ photocatalyst

To prove the successful construction of the amorphous NiB nanodot-loaded TiO₂ photocatalyst, the transmission electron microscopy (TEM) characterization is first conducted and the resulting images are shown in Fig. 3. According to the high-resolution TEM images, it can be apparently found that multiple amorphous NiB nanodots with small size of 0.5–1 nm are homogeneously well-attached onto the TiO₂ surface (Fig. 3a). The above fact can further be verified via the following high-angle annular dark field transmission electron microscopic (HAADF-

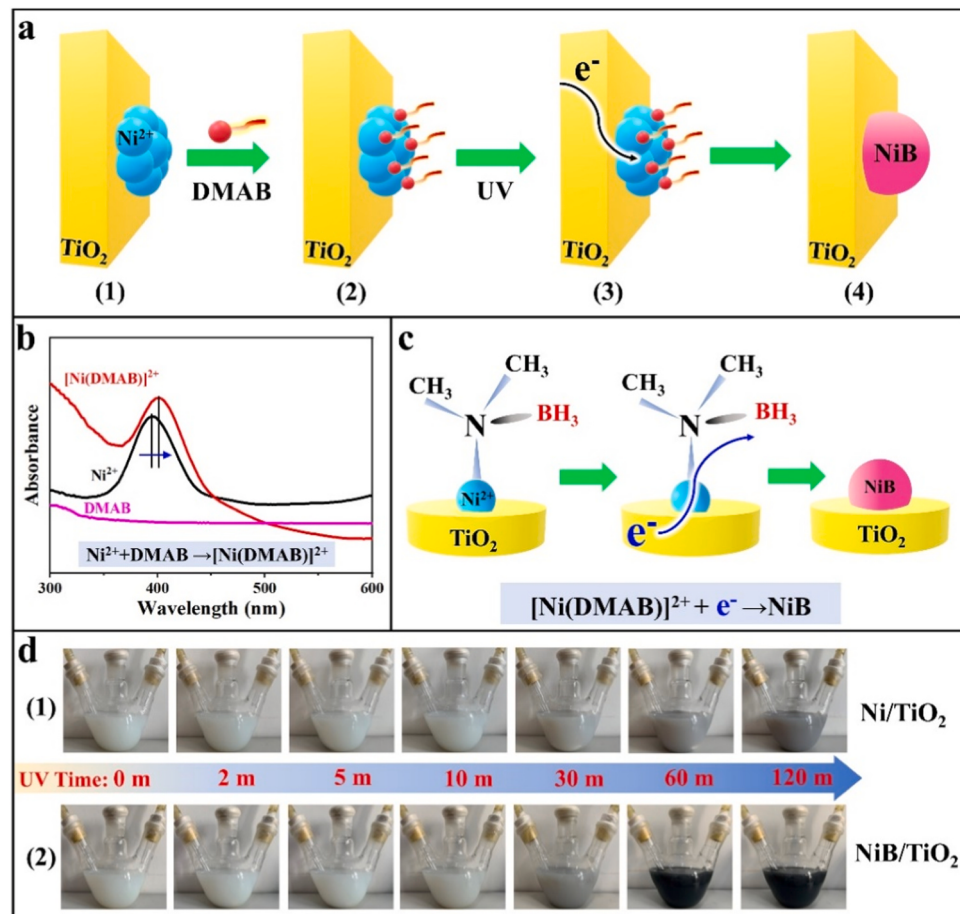


Fig. 2. (a) Graphical illustration for the photosynthesis of a-NiB/TiO₂. (b) The UV-visible adsorption spectra of various solutions. (c) Graphical illustration for the formation mechanism of amorphous NiB triggered by photoexcited electrons. (d) The photographs of the color change in different photodeposition stages: (1) Ni/TiO₂ and (2) a-NiB/TiO₂.

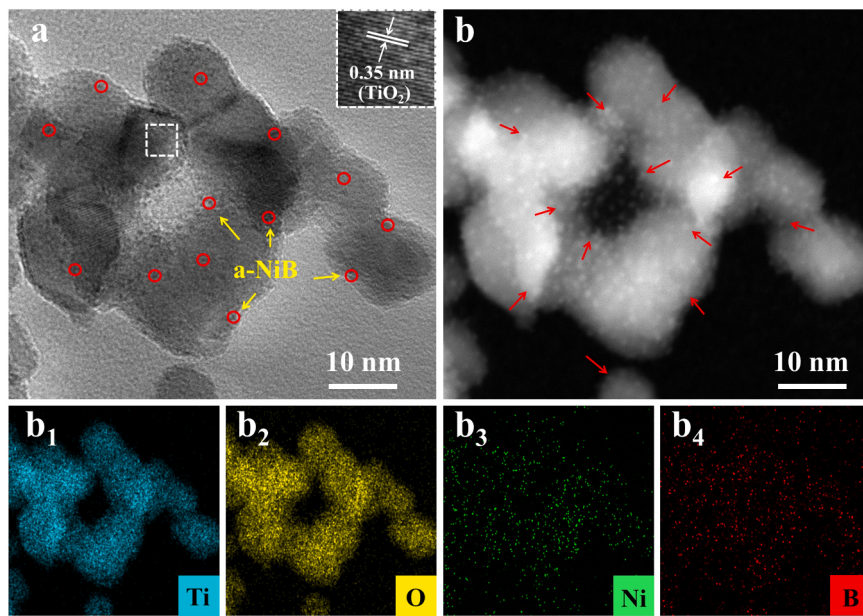


Fig. 3. (a) HRTEM, (b) HAADF-STEM and (b₂–b₄) EDS mapping images of the a-NiB/TiO₂ photocatalyst.

TEM) image in Fig. 3b, where plentiful highlighted amorphous NiB nanodots can be easily identified in the corresponding position. Furthermore, the in-situ element mapping results (Fig. 3b₁–b₄) reveal that the signals of Ni and B elements are well-distributed with the Ti and O elements and the Ni/B ratio is calculated to be 1.6 according to the ICP-OES result, strongly verifying the successful synthesis of amorphous NiB nanodots on TiO₂ surface.

The XRD, SEM, and UV-vis diffuse reflectance characterizations are further employed to evidence the successful preparation of a-NiB/TiO₂ photocatalyst. As the XRD results displayed in Fig. 4a and Fig. S2, all the cocatalyst-modified TiO₂ photocatalysts show the comparable diffraction signal to the bare TiO₂, implying the few influence of present synthetic route on the TiO₂ structure [51,52]. In addition, there is no obvious distinction between the SEM images of a-NiB/TiO₂ and bare TiO₂ (Fig. S3), suggesting that the applied photosynthesis has no effect on the morphology [53]. Significantly, according to the slow-scan XRD results in Fig. 4b, it is obvious that compared to the amorphous NiB/TiO₂ sample, the crystalline NiB/TiO₂ sample obviously shows the characteristic diffraction peak of crystalline Ni₃B (The peak at 44.1° is related to the rutile TiO₂), strongly manifesting the successful crystallization of a-NiB/TiO₂ photocatalyst to form c-NiB/TiO₂ sample. To further reveal the above crystallization of amorphous NiB, the pure a-NiB is first prepared, and then calcined to prepare the crystalline c-NiB

(The detailed processes are shown in SI-1). Based on their XRD patterns, it is obvious that compared with the weak and broad amorphous peak of a-NiB, the c-NiB sample shows the strong and sharp Ni₃B (#48-1223) characteristic peaks, verifying the effective transformation of amorphous NiB to crystalline NiB via the present calcination strategy [54,55]. Furthermore, the UV-vis absorption spectra of various samples are carried out to reveal their optical absorption properties and the results are shown in Fig. 4c. It can be observed that the TiO₂ sample exhibits the absorption boundary of around 390 nm, and the bandgap value can be determined to 3.20 eV (Fig. S5) [56,57]. With the loading of Ni cocatalyst, an obvious enhancement of light absorption (390–700 nm) can be observed, and the color of Ni/TiO₂ sample changes from white to gray (inset in Fig. 3d). When modifying with a-NiB and c-NiB, the resulting a-NiB/TiO₂ and c-NiB/TiO₂ photocatalysts possess further enhanced light absorption and deepened sample color owing to the introduction of black NiB. Moreover, as shown in Fig. S6, with the increase loading amount of a-NiB cocatalyst, the visible light absorption and dark degree of the sample color are gradually increased, indicating that the a-NiB with various loading amount can effectively be modified onto the TiO₂ surface. In summary, the above data strongly verify the successful construction of a-NiB/TiO₂ photocatalyst via the well-designed light-induce deposition procedure.

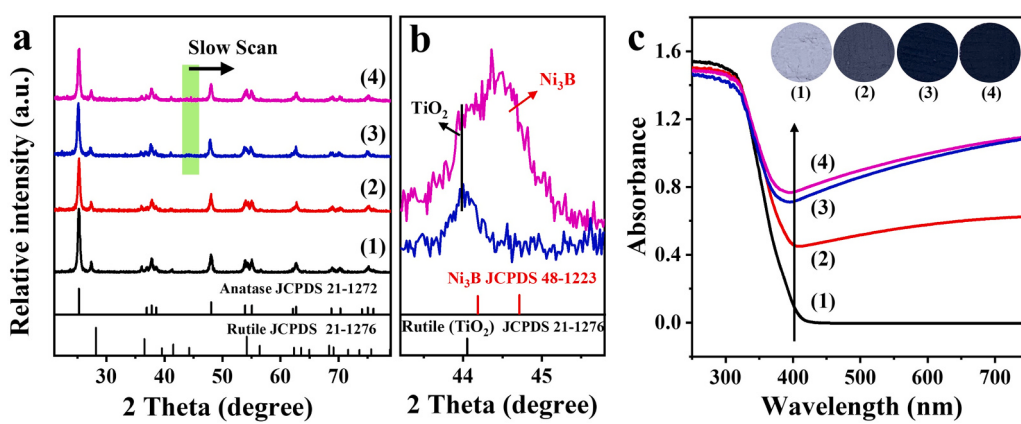


Fig. 4. (a) XRD patterns, (b) slow-scan XRD patterns and (c) UV-vis adsorption spectra of (1) TiO₂, (2) Ni/TiO₂, (3) a-NiB/TiO₂ and (4) c-NiB/TiO₂.

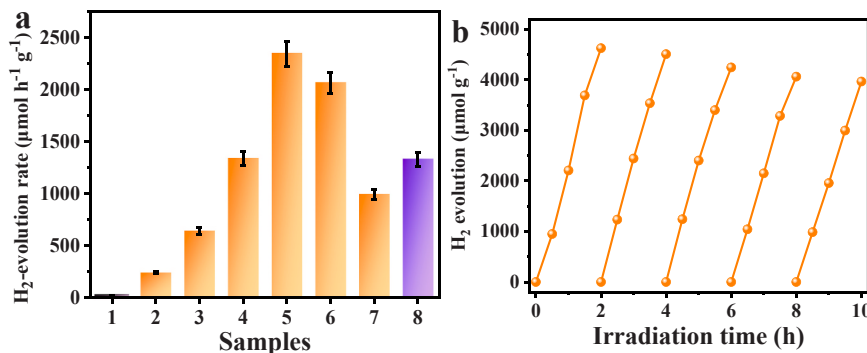


Fig. 5. (a) The photocatalytic H_2 -evolution activity of various samples: (1) TiO_2 , (2) a-NiB/TiO_2 (1 wt%), (3) a-NiB/TiO_2 (3 wt%), (4) a-NiB/TiO_2 (5 wt%), (5) a-NiB/TiO_2 (8 wt%), (6) a-NiB/TiO_2 (10 wt%), (7) a-NiB/TiO_2 (12 wt%) and (8) c-NiB/TiO_2 . (b) The cycling runs of the photocatalytic H_2 -evolution activity of the a-NiB/TiO_2 (8 wt%).

3.3. Photocatalytic H_2 -evolution performance and mechanism

The photocatalytic H_2 -evolution activities of the obtained photocatalysts are accessed under UV light of 365 nm with the presence of LA sacrificial agent (10 vol%), as depicted in Fig. 5. The bare TiO_2

photocatalyst displays the trivial performance of $16.3 \mu\text{mol h}^{-1} \text{g}^{-1}$, which can be ascribed to the rapid recombination of carriers and the ineffective catalytic H_2 -generation sites. When a-NiB cocatalyst is modified onto TiO_2 , it can be obviously found that the synthetic a-NiB/ TiO_2 photocatalysts possess the tremendous enhancement of H_2 -

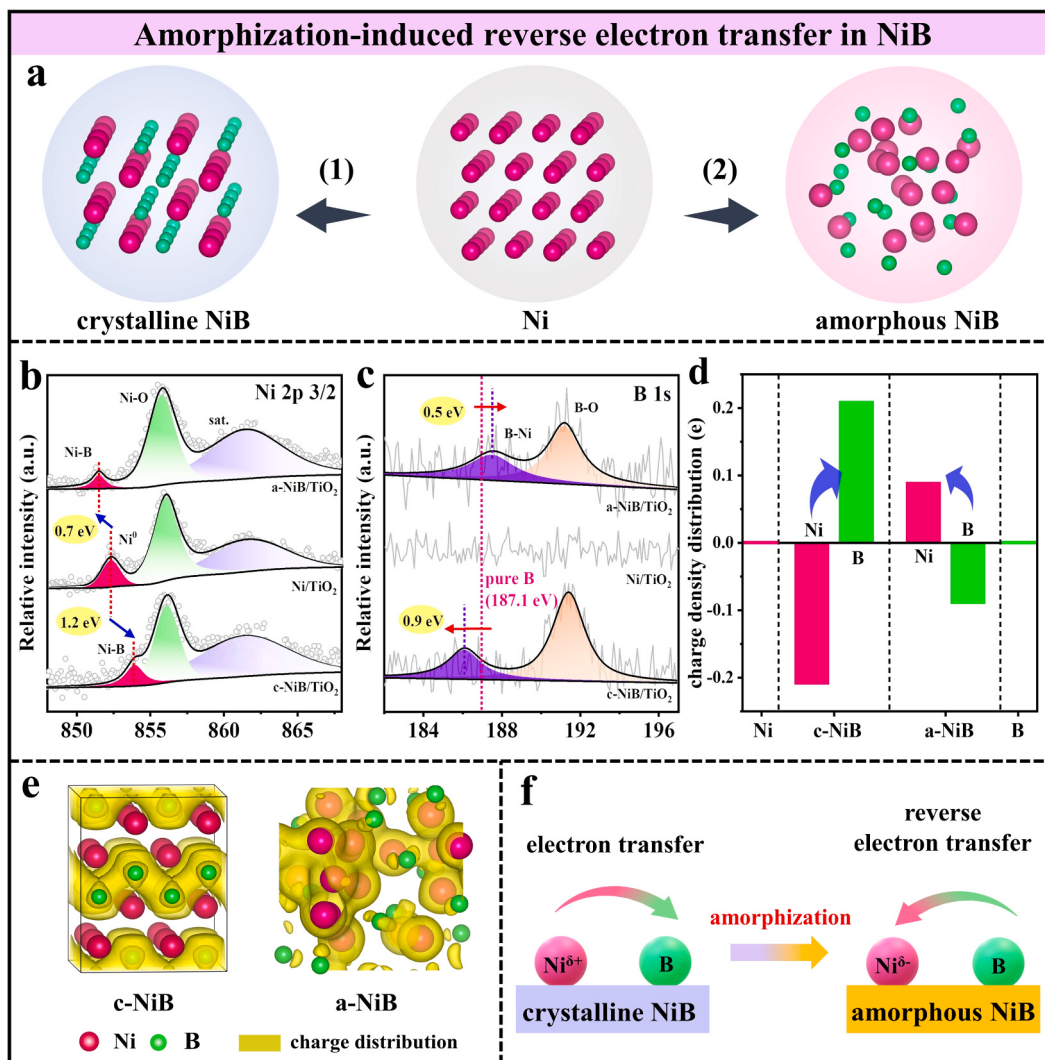


Fig. 6. (a) Schematic illustration for introducing boron to nickel to form (1) c-NiB and (2) a-NiB . (b-c) The fitted high-resolution XPS spectra of Ni 2p and B 1s for Ni/TiO_2 , c-NiB/TiO_2 and a-NiB/TiO_2 . (d) The Bader charge density distributions of c-NiB and a-NiB . (e) The band decomposed charge density distributions in c-NiB and a-NiB . (f) Schematic illustration for the amorphization-induced reverse electron transfer mechanism in NiB.

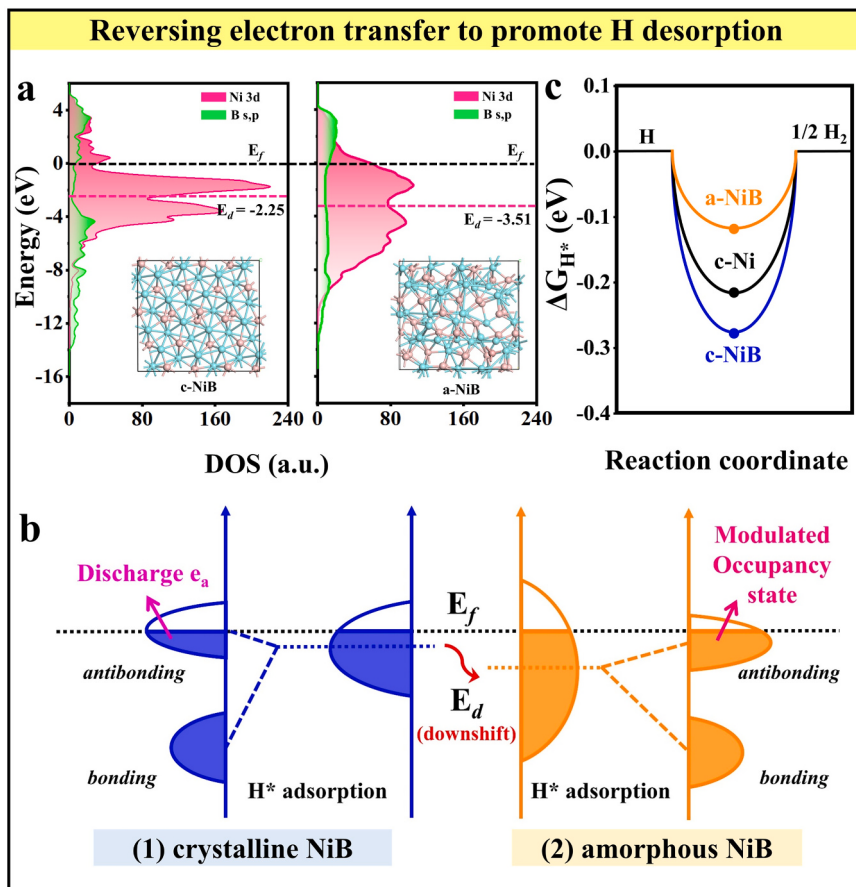


Fig. 7. (a) Calculated pDOS and d-band center of c-NiB (left) and a-NiB (right). (b) Schematic illustration for the tailored antibonding-orbital occupancy state of d-band of Ni active site in crystalline and amorphous NiB. (c) The calculated Gibbs free energy barriers for hydrogen adsorption-desorption balance of Ni sites in Ni, c-NiB and a-NiB.

production performance compared to the bare TiO_2 . Particularly, the a-NiB/ TiO_2 photocatalyst with the loading amount of 8 wt% shows the optimal photocatalytic H_2 -generation activity of $2344.0 \mu\text{mol h}^{-1} \text{g}^{-1}$ with an apparent quantum yield (AQY) of 16.3 % (Table S1). Moreover, the cycling performance experiment is employed to study the H_2 -evolution stability of the a-NiB/ TiO_2 photocatalyst (Fig. 5b), and the activity of a-NiB/ TiO_2 remains stable even after 5 cycling measurements, implying its positive repeatability. Herein, its corresponding turnover number (TON) is calculated to be 42.1 (The detailed calculation is shown in SI-5). It is worth noting that the H_2 -production performance of amorphous NiB/ TiO_2 is apparently higher than that of the crystalline NiB/ TiO_2 ($1330.7 \mu\text{mol h}^{-1} \text{g}^{-1}$), indicating that compared to the crystalline NiB cocatalyst, the amorphization of NiB cocatalyst can effectively boost the photocatalytic H_2 -production activity of TiO_2 . Furthermore, the amorphization strategy of NiB cocatalyst can also efficiently boost the H_2 -evolution activity of g-C₃N₄, implying the potential extensibility of amorphous NiB cocatalyst (Fig. S7). Thus, it is necessary to explore the mechanism of the above crystallinity-dependent activity of NiB cocatalyst in the H_2 -evolution process.

According to the above performance test results, it can be found that the amorphization of NiB cocatalyst can efficiently facilitate the H_2 -generation process, which can be attributed to the amorphization-induced reconstruction of electron density distribution in amorphous NiB. To unravel the electron density distribution in crystalline and amorphous NiB, the chemical environment of each element in metallic Ni, crystalline NiB, and amorphous NiB are carefully studied by XPS characterization. According to the XPS results of Ni 2p in Fig. 6b, the Ni/ TiO_2 sample exhibits two characteristic peaks of Ni at 852.3 eV and 855.7 eV, corresponding to the zerovalent and bivalent Ni, respectively.

When introducing B into Ni to form crystalline NiB cocatalyst (Fig. 6a-(1)), it can be easily found that the resulting c-NiB/ TiO_2 sample show the typical Ni peak at 853.5 eV, which is higher than that of the traditional Ni/ TiO_2 . The above positive shift (1.2 eV) of Ni peak in crystalline NiB can be ascribed to the electron transfer from Ni to B, which is caused by the introduction of B with higher electronegativity than Ni. Interestingly, the above results about electron transfer is completely reversed in the amorphous NiB structure (Fig. 6a-(2)). In this case, compared with the conventional Ni/ TiO_2 sample, the binding energy of Ni peak on the a-NiB/ TiO_2 sample is negatively shifted to 851.6 eV, powerfully proving the fact that the electron of B can reversibly transfer to Ni in the amorphous NiB. In fact, the above-mentioned reverse electron transfer in the amorphous NiB can simultaneously be verified via the XPS results of B 1 s, as shown in Fig. 6c. Comparing with the binding energy of pure B (187.1 eV), the elemental B in c-NiB/ TiO_2 is negatively shifted by 0.9 eV, while the elemental B in a-NiB/ TiO_2 possesses a reversely positive shift of 0.5 eV, which further suggest the phenomenon of amorphization-induced reverse electron transfer in NiB. In addition, the reverse electron transfer mechanism in amorphous NiB can further be theoretically investigated via the following DFT calculation. The crystalline model of c-NiB contains 96 Ni atoms and 72 B atoms, and the atomic ratio of B to Ni is 0.75 (the value is approximate to the ICP-OES result of a-NiB/ TiO_2). Furthermore, the amorphous model of a-NiB is reasonably constructed using a wide-accept “melt-and-quench” approach based on the above c-NiB model via dynamic simulation and geometric optimization, and the optimized models are shown in Fig. S8 (The detailed processes are shown in SI-8). First, as displayed in Fig. 6d, the Bader charge analysis is employed to quantitatively explore the electron transfer between Ni and B atom in crystalline and amorphous

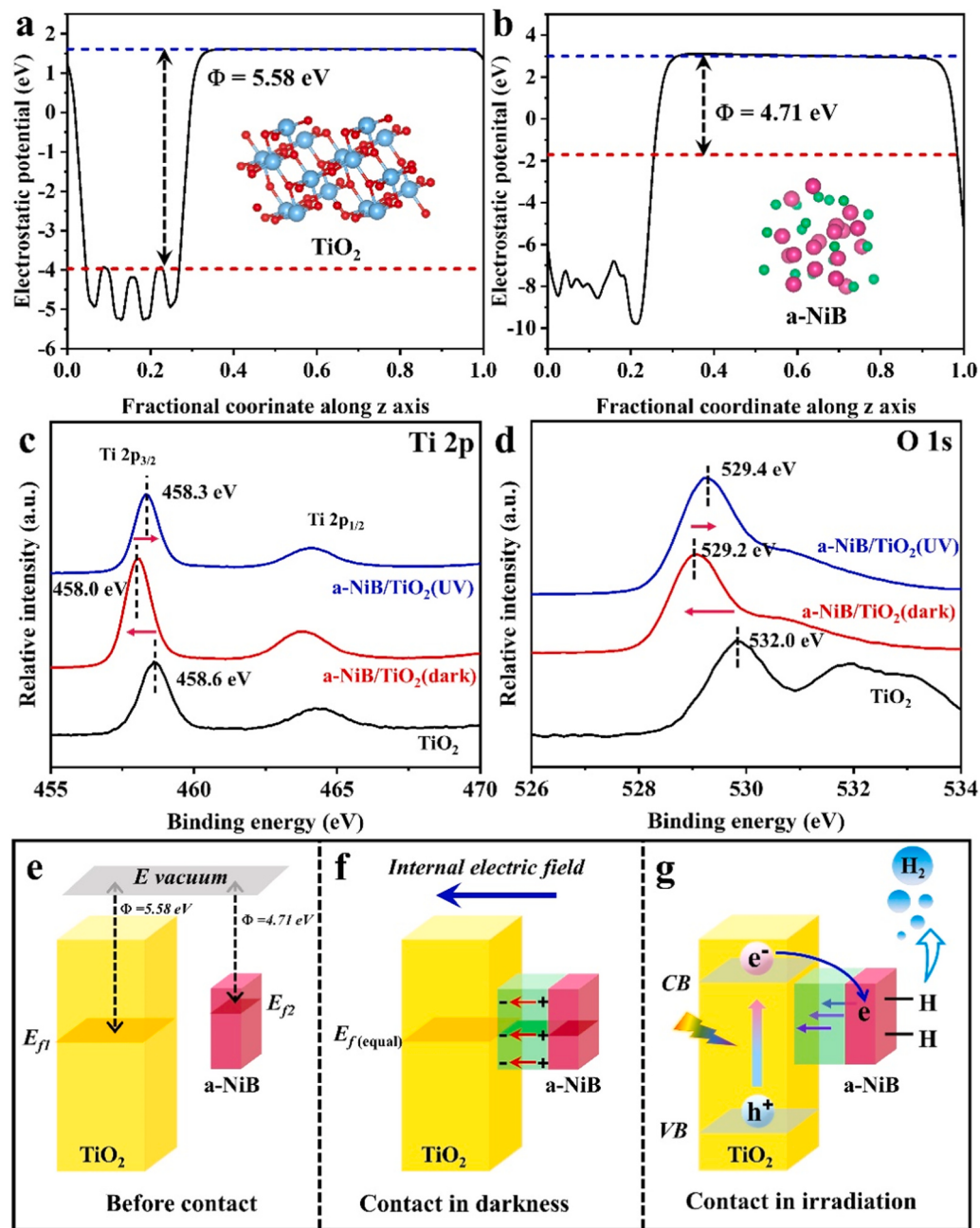


Fig. 8. (a-b) Calculated electrostatic potentials for TiO_2 photocatalyst and a-NiB cocatalyst. (c-d) In-situ XPS results of Ti 2p and O 1s for TiO_2 , a-NiB/TiO₂ (dark), and a-NiB/TiO₂ (UV). (e-g) Schematic diagram for the promoted photoelectron transfer from TiO_2 to a-NiB under the enforcement of internal electric field.

NiB. The calculated Bader charge results indicate that Ni atom averagely losses 0.21 electrons ($|\epsilon|$) to B in crystalline NiB, but for the amorphous NiB, the Ni atom can conversely gain 0.09 electrons from B, reconfirming the amorphization-induced reverse electron transfer in NiB. Furthermore, the above reverse electron transfer can be visually observed via the band decomposed charge density distributions analysis (Fig. 6e). Clearly, it can be found that compared with the crystalline NiB structure, the simulated charge distribution is mainly accumulated on the Ni site in the amorphous NiB structure, which is in line with the above XPS and Bader charge analysis results. Therefore, based on the above experimental and theoretical results, it can be rationally authenticated the amorphization-induced reverse electron transfer mechanism in NiB, as depicted in Fig. 6f.

The above amorphization-induced reverse electron transfer can effectively adjust the electronic configuration of Ni active site in a-NiB to

promote the interfacial H_2 -desorption process, thereby boosting the H_2 -evolution activity, which can be well investigated via the following projected density of states (pDOS) analysis and ΔG_{H^+} calculation. Based on the pDOS results of c-NiB and a-NiB in Fig. 7a, the d-band of Ni atoms is obviously localized near the fermi level compared with that of s,p-band of B atoms, suggesting that the Ni sites of NiB cocatalyst act as the active site for hydrogen production. Moreover, the above exploration of active sites in NiB can be well achieved via the electrochemical in situ shielding approach (Fig. S9). In this case, after the poison of Ni sites, the current density of NiB greatly decreases, implying that Ni is the feasible active site for photocatalytic H_2 evolution in NiB cocatalyst. Further analysis of the pDOS suggested that compared with the crystalline structure, the amorphous NiB clearly displays a relatively broad and diffused d-band of Ni, which can be ascribed to the strengthened orbital hybridization between Ni 3d and B 2s-2p states induced by its

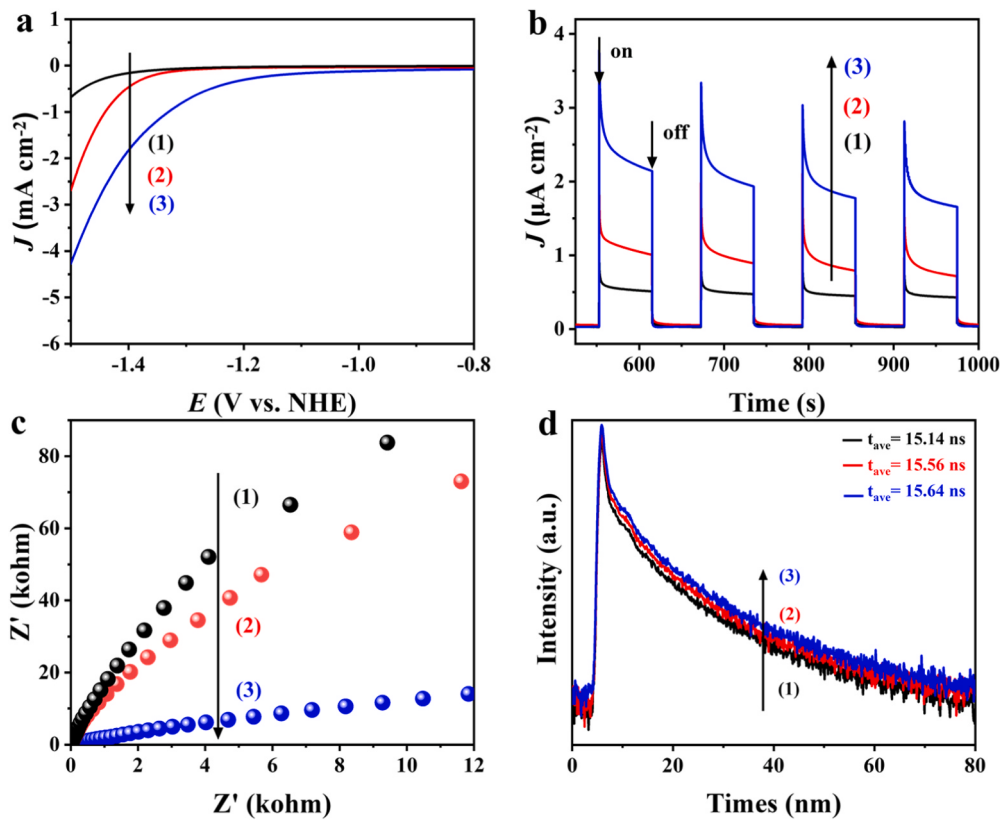


Fig. 9. (a) linear sweep voltammetry (LSV), (b) transient photocurrent response curves, (c) electrochemical impedance spectra (EIS) and (d) transient-state photoluminescence spectra of (1) TiO_2 , (2) c-NiB/TiO₂, and (3) a-NiB/TiO₂.

disordered coordination environment. In this contribution, based on the d-band theory as shown in Fig. S10, the broadening of d-band in amorphous NiB can significantly induce the downshift of the d-band center of Ni, which is in line with the present calculated results of d-band center (-2.25 eV for c-NiB and -3.51 eV for a-NiB). As a result, with the downshift of the d-band center, the antibonding orbitals formed through the interaction of Ni-H_{ads} can be filled by more electrons (Fig. 7b), leading to the promotion of H₂ desorption on Ni active site, thereby boosting the H₂-evolution activity of the amorphous NiB cocatalyst. Furthermore, based on the simulated surface models of a-NiB and c-NiB in Fig. S11, the free energy change calculation on Ni active site is conducted, as shown in Fig. 7c. As for c-NiB cocatalyst, the ΔG_{H^*} of Ni site exhibits an adverse value of -0.282 eV due to the electron transfer from Ni to B, which can induce the decrease of electron density of Ni site, therefore inhibiting the hydrogen desorption process. After amorphization to form NiB cocatalyst, the ΔG_{H^*} of Ni site is obviously optimized to -0.138 eV, indicating the weakening of hydrogen adsorption on Ni, which can boost hydrogen desorption to promote the H₂-evolution performance. Therefore, it can be concluded that the amorphization-induced reverse electron of a-NiB can modulate the antibonding orbital occupation state of Ni active site to boost the hydrogen desorption process, thereby promoting the interfacial hydrogen evolution reaction.

Aside from boosting interfacial hydrogen evolution reaction, the a-NiB cocatalyst can also efficiently boost the separation of photo-generated electrons, which is investigated via the following DFT calculation and in-situ irradiated XPS characterization (Fig. 8). Based on the DFT results in Fig. 8a-b, the calculated work functions (Φ) of TiO_2 and a-NiB are identified to 5.58 and 4.71 eV, respectively (Fig. 8e). When TiO_2 nanoparticles and a-NiB nanodots are contacted in darkness, their E_f difference can induce the migration of free electrons from a-NiB to TiO_2 , which can be well evidenced by the negative shift of the Ti 2p and O 1s

XPS signals (Fig. 8c-d). As a result of the electron transfer from a-NiB to TiO_2 , an internal electric field directing from a-NiB to TiO_2 is successfully constructed at their interface (Fig. 8f). When the a-NiB/TiO₂ photocatalyst is irradiated by UV light, the above-constructed internal electric field can effectively boost the separation and transmission of photogenerated electrons to a-NiB cocatalyst, which can be revealed by the in-situ irradiated XPS results in Fig. 8b-c and Fig. S12a-b. In this case, compared with the a-NiB/TiO₂ (dark), the binding energies of Ti (Fig. 8c) and O (Fig. 8d) elements in a-NiB/TiO₂ (light) shift to a higher value, while the Ni (Fig. S12a) and B (Fig. S12b) elements exhibit a negative shift, strongly demonstrating the flow of the light-excited electrons from TiO_2 to a-NiB cocatalyst during the photocatalytic procedure. Therefore, it can be firmly concluded that the photogenerated electrons of TiO_2 can be easily transferred to the a-NiB cocatalyst to boost the interfacial hydrogen generation (Fig. 8g).

The fast transport of photoexcited electrons and promoted interfacial H₂-evolution efficiency of a-NiB/TiO₂ photocatalyst can further be evidenced via photoelectrochemical measurements and transient-state photoluminescence (PL) spectra (Fig. 9). Based on the LSV curves in Fig. 9a, the current density of the a-NiB/TiO₂ photocatalyst is obviously larger than that of c-NiB/TiO₂ and bare TiO_2 , indicating that the amorphization of NiB cocatalyst can boost the hydrogen-production process. In addition, based on the results of transient photocurrent response (Fig. 9b), electrochemical impedance (Fig. 9c), and TRPL (Fig. 9d), the a-NiB/TiO₂ sample shows the maximal photocurrent density, minimum impedance, and longest fluorescent lifetime in contrast with other samples, adequately implying the efficient separation and transportation of charges in the a-NiB/TiO₂ photocatalyst. Thus, the foregoing data demonstrated that the amorphous NiB cocatalyst can efficiently separate and transport photogenerated electrons of TiO_2 to achieve the promoted interfacial H₂-generation process.

4. Conclusions

To summarize, amorphous NiB nanodots were successfully fabricated and perfectly anchored onto TiO_2 surface via a well-designed photoinduced route. Photocatalytic H_2 -evolution tests supported that the as-formed a-NiB/ TiO_2 shows the superior activity of $2334.0 \mu\text{mol h}^{-1} \text{ g}^{-1}$, which is 1.8 times over the traditional c-NiB/ TiO_2 photocatalyst. The theoretical and experimental results evidenced that the amorphization of NiB cocatalyst can induce the reverse electron transfer from B to Ni, therefore increasing the electron density of Ni active site to optimize its hydrogen desorption process. Consequently, the a-NiB nanodots can work as the effective cocatalyst to fastly transport the photoexcited electron to boost the interfacial H_2 -production reaction, thereby enhancing the photocatalytic H_2 -production activity of TiO_2 . This work not only offers a new method for the synthesis of metal boride-based cocatalysts, but also suggests the amorphization-induced optimization of active sites for hydrogen production.

CRediT authorship contribution statement

Haoyu Long: Methodology, Validation, Writing – original draft. **Duoduo Gao:** Investigation, Visualization. **Ping Wang:** Project administration. **Xuefei Wang:** Data curation, Supervision. **Feng Chen:** Software. **Huogen Yu:** Conceptualization, Resources, Funding acquisition, Writing – review & editing.

Declaration of Competing Interest

The authors declare that they have no known competing financial interests or personal relationships that could have appeared to influence the work reported in this paper.

Data availability

Data will be made available on request.

Acknowledgements

This work was supported by National Natural Science Foundation of China (22178275, U22A20147, and 22075220) and the Natural Science Foundation of Hubei Province of China (2022CFA001).

Appendix A. Supporting information

Supplementary data associated with this article can be found in the online version at [doi:10.1016/j.apcatb.2023.123270](https://doi.org/10.1016/j.apcatb.2023.123270).

References

- [1] Y. Guo, Q. Zhou, J. Nan, W. Shi, F. Cui, Y. Zhu, Perylenetetracarboxylic acid nanosheets with internal electric fields and anisotropic charge migration for photocatalytic hydrogen evolution, *Nat. Commun.* 13 (2022) 2067.
- [2] Y. Hu, X. Yu, Q. Liu, L. Wang, H. Tang, Highly metallic Co-doped MoS_2 nanosheets as an efficient cocatalyst to boost photoredox dual reaction for H_2 production and benzyl alcohol oxidation, *Carbon* 188 (2022) 70.
- [3] J. Liu, W. Fu, Y. Liao, J. Fan, Q. Xiang, Recent advances in crystalline carbon nitride for photocatalysis, *J. Mater. Sci. Technol.* 91 (2021) 224.
- [4] X. Li, Y. Chen, Y. Tao, L. Shen, Z. Xu, Z. Bian, H. Li, Challenges of photocatalysis and their coping strategies, *Chem. Catal.* 2 (2022) 1315.
- [5] Y. Zhao, C. Shao, Z. Lin, S. Jiang, S. Song, Low-energy facets on CdS allomorphic junctions with optimal phase ratio to boost charge directional transfer for photocatalytic H_2 fuel evolution, *Small* 16 (2020), 2000944.
- [6] Y. Kondo, Y. Kuwahara, K. Mori, H. Yamashita, Design of metal-organic framework catalysts for photocatalytic hydrogen peroxide production, *Chem* 8 (2022) 2924.
- [7] F. Li, L. Cheng, J. Fan, Q. Xiang, Steering the behavior of photogenerated carriers in semiconductor photocatalysts: a new insight and perspective, *J. Mater. Chem. A* 9 (2021) 23765.
- [8] X. Li, Y. Chen, Y. Tao, L. Shen, Z. Xu, Z. Bian, H. Li, Challenges of photocatalysis and their coping strategies, *Chem. Catal.* 2 (2022) 1315.
- [9] H. Zhao, Q. Mao, L. Jian, Y. Dong, Y. Zhu, , Photodeposition of earth-abundant cocatalysts in photocatalytic water splitting: methods, functions, and mechanisms, *Chin. J. Catal.* 43 (2022) 1774.
- [10] Y. Yamazaki, T. Toyonaga, N. Doshita, K. Mori, Y. Kuwahara, S. Yamazaki, H. Yamashita, Crystal facet engineering and hydrogen spillover-assisted synthesis of defective Pt/ TiO_{2-x} nanorods with enhanced visible light-driven photocatalytic activity, *ACS Appl. Mater. Interfaces* 14 (2022) 2291.
- [11] R. Li, X. Ou, L. Zhang, Z. Qi, X. Wu, C. Lu, J. Fan, K. Lv, Photocatalytic oxidation of NO on reduction type semiconductor photocatalysts: effect of metallic Bi on CdS nanorods, *Chem. Commun.* 57 (2021) 10067.
- [12] J. Xu, W. Zhong, F. Chen, X. Wang, H. Yu, In situ cascade growth-induced strong coupling effect toward efficient photocatalytic hydrogen evolution of $\text{ReS}_2/\text{ZnIn}_2\text{S}_4$, *Appl. Catal. B Environ.* 328 (2023), 122493.
- [13] G. Yao, S. Yang, J. He, S. Jiang, C. Sun, S. Song, In situ growing graphene on $\text{g-C}_3\text{N}_4$ with barrier-free interface and polarization electric field for strongly boosting solar energy conversion into H_2 energy, *Appl. Catal. B Environ.* 287 (2021), 119986.
- [14] M. Li, M. Wei, X. Xie, Q. Dong, Q. Gao, X. Cai, S. Zhang, F. Peng, Y. Fang, S. Yang, Ni foam supported TiO_2 nanorod arrays with CdS branches: type II and Z-scheme mechanisms coexisted monolithic catalyst film for improved photocatalytic H_2 production, *Sol. RRL* 6 (2022), 220018.
- [15] W. Zhong, B. Zhao, X. Wang, P. Wang, H. Yu, Synchronously enhancing water adsorption and strengthening Se-H_{ads} bonds in Se-Rich RuSe_{2+x} cocatalyst for efficient alkaline photocatalytic H_2 production, *ACS Catal.* 13 (2022) 749.
- [16] H. Wang, H. Qi, X. Sun, S. Jia, X. Li, T. Miao, L. Xiong, S. Wang, X. Zhang, X. Liu, A. Wang, T. Zhang, W. Huang, J. Tang, High quantum efficiency of hydrogen production from methanol aqueous solution with PtCu-TiO_2 photocatalysts, *Nat. Mater.* 22 (2023) 619.
- [17] T.H. Tan, B. Xie, Y.H. Ng, S.F.B. Abdullah, H.Y.M. Tang, N. Bedford, R.A. Taylor, K.-F. Aguey-Zinsou, R. Amal, J. Scott, Unlocking the potential of the formate pathway in the photo-assisted sabatier reaction, *Nat. Catal.* 3 (2020) 1034.
- [18] D. Gao, J. Xu, L. Wang, B. Zhu, H. Yu, J. Yu, Optimizing atomic hydrogen desorption of sulfur-rich NiS_{1+x} cocatalyst for boosting photocatalytic H_2 evolution, *Adv. Mater.* 34 (2022), 2108475.
- [19] Q. Dong, M. Li, M. Sun, F. Si, Q. Gao, X. Cai, Y. Xu, T. Yuan, S. Zhang, F. Peng, Y. Fang, S. Yuan, Phase-controllable growth Ni_xPy modified CdS @ Ni_3S_2 electrodes for efficient electrocatalytic and enhanced photoassisted electrocatalytic overall water splitting, *Small Methods* 5 (2021), 2100878.
- [20] L. Cheng, P. Zhang, Q. Wen, J. Fan, Q. Xiang, Copper and platinum dual-single-atoms supported on crystalline graphitic carbon nitride for enhanced photocatalytic CO_2 reduction, *Chin. J. Catal.* 43 (2022) 451.
- [21] J. Tao, X. Yu, Q. Liu, G. Liu, H. Tang, Internal electric field induced S-scheme heterojunction $\text{MoS}_2/\text{CoAl LDH}$ for enhanced photocatalytic hydrogen evolution, *J. Colloid Interface Sci.* 585 (2021) 470.
- [22] J. Xu, D. Gao, H. Yu, P. Wang, B. Zhu, L. Wang, J. Fan, Palladium-copper nanodot as novel H_2 -evolution cocatalyst: optimizing interfacial hydrogen desorption for highly efficient photocatalytic activity, *Chin. J. Catal.* 43 (2022) 215.
- [23] V.G. Nair, M. Birowska, D. Bury, M. Jakubczak, A. Rosenkranz, A.M. Jastrzebska, 2D MBenes: a novel member in the flatland, *Adv. Mater.* 34 (2022), 2108840.
- [24] X. Ai, X. Zou, H. Chen, Y. Su, X. Feng, Q. Li, Y. Liu, Y. Zhang, X. Zou, Transition-metal-boron intermetallics with strong interatomic d-sp orbital hybridization for high-performance electrocatalysis, *Angew. Chem. Int. Ed.* 59 (2020) 3961.
- [25] Q. Li, X. Zou, X. Ai, H. Chen, L. Sun, X. Zou, Revealing activity trends of metal diborides toward pH-universal hydrogen evolution electrocatalysts with Pt-like activity, *Adv. Energy Mater.* 9 (2018), 1803369.
- [26] W. Xiong, X. Feng, Y. Xiao, T. Huang, X. Li, Z. Huang, S. Ye, Y. Li, X. Ren, X. Wang, X. Ouyang, Q. Zhang, J. Liu, Fluorine-free prepared two-dimensional molybdenum boride (MBene) as a promising anode for lithium-ion batteries with superior electrochemical performance, *Chem. Eng. J.* 446 (2022), 137466.
- [27] J. Wu, M. Hou, Z. Chen, W. Hao, X. Pan, H. Yang, W. Cen, Y. Liu, H. Huang, P. W. Menezes, Z. Kang, Composition engineering of amorphous nickel boride nanoarchitectures enabling highly efficient electrosynthesis of hydrogen peroxide, *Adv. Mater.* 34 (2022), 2202995.
- [28] X. Chen, Z. Yu, L. Wei, Z. Zhou, S. Zhai, J. Chen, Y. Wang, Q. Huang, H.E. Karahan, X. Liao, Y. Chen, Ultrathin nickel boride nanosheets anchored on functionalized carbon nanotubes as bifunctional electrocatalysts for overall water splitting, *J. Mater. Chem. A* 7 (2019) 764.
- [29] Y. Chen, T. Zhou, L. Li, W.K. Pang, X. He, Y.N. Liu, Z. Guo, Interfacial engineering of nickel boride/metaborate and its effect on high energy density asymmetric supercapacitors, *ACS Nano* 13 (2019) 9376.
- [30] J. Masa, I. Sinev, H. Mistry, E. Ventosa, M. de la Mata, J. Arbiol, M. Muhler, B. Roldan Cuena, W. Schuhmann, Ultrathin high surface area nickel boride (Ni_xB) nanosheets as highly efficient electrocatalyst for oxygen evolution, *Adv. Energy Mater.* 7 (2017), 1700381.
- [31] X. Li, S. Lu, J. Yi, L. Shen, Z. Chen, H. Xue, Q. Qian, M.Q. Yang, Ultrathin two-dimensional $\text{ZnIn}_2\text{S}_4/\text{Ni}_x\text{B}$ heterostructure for high-performance photocatalytic fine chemical synthesis and H_2 generation, *ACS Appl. Mater. Interfaces* 14 (2022) 25297.
- [32] H. Long, P. Wang, X. Wang, F. Chen, H. Yu, Optimizing hydrogen adsorption of Ni_xB cocatalyst by integrating P atom for enhanced photocatalytic H_2 -production activity of CdS , *Appl. Surf. Sci.* 604 (2022), 154457.
- [33] K. Wang, H. Yang, J. Zhang, G. Ren, T. Cheng, Y. Xu, X. Huang, The exclusive surface and electronic effects of Ni on promoting the activity of Pt towards alkaline hydrogen oxidation, *Nano Res.* 15 (2022) 5865.
- [34] D. Gao, W. Zhong, Y. Liu, H. Yu, J. Fan, Synergism of tellurium-rich structure and amorphization of NiTe_{1-x} nanodots for efficient photocatalytic H_2 -evolution, *Appl. Catal. B Environ.* 290 (2021), 120057.

[35] S. Dong, Y. Pu, Y. Niu, L. Zhang, Y. Wang, B. Zhang, Interstitial carbon in Ni enables high-efficiency hydrogenation of 1,3-Butadiene, *Acta Phys. Chim. Sin* 39 (2023), 2301012.

[36] D. Gao, P. Deng, J. Zhang, L. Zhang, X. Wang, H. Yu, J. Yu, Reversing free-electron transfer of MoS_2+x cocatalyst for optimizing antibonding-orbital occupancy enables high photocatalytic H_2 evolution, *Angew. Chem. Int. Ed.* 62 (2023), 202304559.

[37] F. Ma, S. Wang, X. Liang, C. Wang, F. Tong, Z. Wang, P. Wang, Y. Liu, Y. Dai, Z. Zheng, B. Huang, Ni_3B as a highly efficient and selective catalyst for the electrosynthesis of hydrogen peroxide, *Appl. Catal. B Environ.* 279 (2020) 11371.

[38] W. Jiang, S. Niu, T. Tang, Q. Zhang, X. Liu, Y. Zhang, Y. Chen, J. Li, L. Gu, L. Wan, J. Hu, Crystallinity-modulated electrocatalytic activity of a nickel (II) borate thin layer on Ni_3B for efficient water oxidation, *Angew. Chem. Int. Ed.* 56 (2017) 6572.

[39] W. Hao, R. Wu, H. Yang, Y. Guo, Photothermal coupling electrolysis on Ni-W-B toward practical overall water splitting, *J. Mater. Chem. A* 7 (2019) 12440.

[40] Y. Li, W. Zhang, H. Li, T. Yang, S. Peng, C. Kao, Ni-B coupled with borate-intercalated Ni(OH)_2 for efficient and stable electrocatalytic and photocatalytic hydrogen evolution under low alkalinity, *Chem. Eng. J.* 394 (2020), 124928.

[41] F. Yang, P. Han, N. Yao, G. Cheng, S. Chen, W. Luo, Inter-regulated d-band centers of the $\text{Ni}_3\text{B}/\text{Ni}$ heterostructure for boosting hydrogen electrooxidation in alkaline media, *Chem. Sci.* 11 (2020) 12118.

[42] Y. Qi, Y. Zhang, L. Yang, Y. Zhao, Y. Zhu, H. Jiang, C. Li, Insights into the activity of nickel boride/nickel heterostructures for efficient methanol electrooxidation, *Nat. Commun.* 13 (2022) 4602.

[43] H. Huang, H. Jung, H. Jun, D.Y. Woo, J.W. Han, J. Lee, Design of grain boundary enriched bimetallic borides for enhanced hydrogen evolution reaction, *Chem. Eng. J.* 405 (2021), 126977.

[44] L. Li, Z. Deng, L. Yu, Z. Lin, W. Wang, G. Yang, Amorphous transitional metal borides as substitutes for Pt cocatalysts for photocatalytic water splitting, *Nano Energy* 27 (2016) 103.

[45] C. Shan, Z. Chen, R. Wang, M. Liu, L. Zhao, T. Bold, Design and microstructural development of a new eutectic Fe-Co-Ni-B multi-principal element alloy system, *J. Alloy. Compd.* 897 (2022), 163205.

[46] S. Dutta, H. Han, M. Je, H. Choi, J. Kwon, K. Park, A. Indra, K.M. Kim, U. Paik, T. Song, Chemical and structural engineering of transition metal boride towards excellent and sustainable hydrogen evolution reaction, *Nano Energy* 67 (2020), 104245.

[47] Y.M. He, L.R. Liu, C. Zhu, S.S. Guo, P. Golani, B. Koo, P.Y. Tang, Z.Q. Zhao, M. Z. Xu, P. Yu, X. Zhou, C.T. Gao, X.W. Wang, Z.D. Shi, L. Zheng, J.F. Yang, B. Shin, J. Arbiol, H.G. Duan, Y.H. Du, M. Heggen, R.E. Dunin-Borkowski, W.L. Guo, Q. J. Wang, Z.H. Zhang, Z. Liu, Amorphizing noble metal chalcogenide catalysts at the single-layer limit towards hydrogen production, *Nat. Catal.* 5 (2022) 212.

[48] P. Gomathisankar, D. Yamamoto, H. Katsumata, T. Suzuki, S. Kaneko, Photocatalytic hydrogen production with aid of simultaneous metal deposition using titanium dioxide from aqueous glucose solution, *Int. J. Hydrog. Energy* 38 (2013) 5517.

[49] D. Gao, H. Long, X. Wang, J. Yu, H. Yu, Tailoring antibonding-orbital occupancy state of selenium in Se-enriched ReSe_{2+x} cocatalyst for exceptional H_2 evolution of TiO_2 photocatalyst, *Adv. Funct. Mater.* 33 (2023), 2209994.

[50] Y. Kang, B. Jiang, J. Yang, Z. Wan, J. Na, Q. Li, H. Li, J. Henzie, Y. Sakka, Y. Yamauchi, T. Asahi, Amorphous alloy architectures in pore walls: mesoporous amorphous NiCoB alloy spheres with controlled compositions via a chemical reduction, *ACS Nano* 14 (2020) 17224.

[51] W. Zhong, X. Wu, Y. Liu, X. Wang, J. Fan, H. Yu, Simultaneous realization of sulfur-rich surface and amorphous nanocluster of NiS_{1+x} cocatalyst for efficient photocatalytic H_2 evolution, *Appl. Catal. B Environ.* 280 (2021), 119455.

[52] F. Xu, K. Meng, S. Cao, C. Jiang, T. Chen, J. Xu, J. Yu, Step-by-step mechanism insights into the $\text{TiO}_2/\text{Ce}_2\text{S}_3$ S-Scheme photocatalyst for enhanced aniline production with water as a proton source, *ACS Catal.* 12 (2022) 164.

[53] W. Zhong, J. Xu, X. Zhang, J. Zhang, X. Wang, H. Yu, Tailoring antibonding-orbital occupancy state of selenium in Se-enriched ReSe_{2+x} cocatalyst for exceptional H_2 evolution of TiO_2 photocatalyst, *Adv. Funct. Mater.* 33 (2023), 2302325.

[54] X. Xu, Y. Deng, M. Gu, B. Sun, Z. Liang, Y. Xue, Y. Guo, J. Tian, H. Cui, Large-scale synthesis of porous nickel boride for robust hydrogen evolution reaction electrocatalyst, *Appl. Surf. Sci.* 470 (2019) 591.

[55] H. Liu, C. Fang, Y. Fang, Y. Zhou, F. Zhu, H. Ge, Z. Yang, Y. Tang, EXAFS study of the structure of amorphous nickel borate, *Acta Phys. Chim. Sin.* 30 (2014) 1979.

[56] P. Wang, H. Li, Y. Cao, H. Yu, Carboxyl-functionalized graphene for highly efficient H_2 -evolution activity of TiO_2 photocatalyst, *Acta Phys. Chim. Sin.* 37 (2021), 2008047.

[57] Q. Zhang, J. Zhang, X. Wang, L. Li, Y.-F. Li, W.-L. Dai, In-N-In sites boosting interfacial charge transfer in carbon-coated hollow tubular $\text{In}_2\text{O}_3/\text{ZnIn}_2\text{S}_4$ heterostructure derived from In-MOF for enhanced photocatalytic hydrogen evolution, *ACS Catal.* 11 (2021) 6276.